

NANOTECHNOLOGY

HfSe₂ and ZrSe₂: Two-dimensional semiconductors with native high- κ oxides

Michal J. Mleczko,¹ Chaofan Zhang,^{2,3*} Hye Ryoung Lee,^{1,4} Hsueh-Hui Kuo,^{3,4}
Blanka Magyari-Köpe,¹ Robert G. Moore,³ Zhi-Xun Shen,^{2,3,5} Ian R. Fisher,^{3,5}
Yoshio Nishi,^{1,4} Eric Pop^{1,4,6†}

The success of silicon as a dominant semiconductor technology has been enabled by its moderate band gap (1.1 eV), permitting low-voltage operation at reduced leakage current, and the existence of SiO₂ as a high-quality “native” insulator. In contrast, other mainstream semiconductors lack stable oxides and must rely on deposited insulators, presenting numerous compatibility challenges. We demonstrate that layered two-dimensional (2D) semiconductors HfSe₂ and ZrSe₂ have band gaps of 0.9 to 1.2 eV (bulk to monolayer) and technologically desirable “high- κ ” native dielectrics HfO₂ and ZrO₂, respectively. We use spectroscopic and computational studies to elucidate their electronic band structure and then fabricate air-stable transistors down to three-layer thickness with careful processing and dielectric encapsulation. Electronic measurements reveal promising performance (on/off ratio > 10⁶; on current, ~30 μ A/ μ m), with native oxides reducing the effects of interfacial traps. These are the first 2D materials to demonstrate technologically relevant properties of silicon, in addition to unique compatibility with high- κ dielectrics, and scaling benefits from their atomically thin nature.

INTRODUCTION

For over five decades, silicon has been the mainstream semiconductor for electronics due to its abundance, control of resistivity by doping, moderate band gap, and its high-quality “native” insulator, SiO₂ (1). In particular, the latter two properties are fundamentally responsible for enabling the efficient, low-power operation of modern silicon processors from mobile electronics to data centers. The 1.1-eV band gap is sufficiently low to allow low-voltage operation (dynamic power dissipation in logic circuits scales as the square of voltage) but sufficiently high to limit direct tunneling and leakage currents (2, 3). The large, 9-eV band gap of the SiO₂ insulator and its high-quality interface with silicon are perhaps even more important in terms of enabling the isolation of silicon components and the reduction of additional gate leakage currents. This combination of properties has been difficult to replicate in other semiconductors, including Ge or compound III-V materials, despite more than half a century of research.

In the last decade, even SiO₂ has been gradually replaced in silicon electronics by the so-called “high- κ ” insulators, which have higher relative dielectric constant values ($\kappa = 16$ to 20 instead of ~4 for SiO₂) and thus can be made physically thicker while maintaining the same capacitance and lower leakage (4, 5). Thus, if silicon has benefited so intimately from its native SiO₂ insulator, then it is important to ask whether well-known high- κ dielectrics, such as HfO₂ or ZrO₂, are native to semiconductors which may themselves be suitable for nanoelectronics. Here, we demonstrate that layered, two-dimensional (2D) semiconductors HfSe₂ and ZrSe₂ satisfy these criteria, being compatible with desirable high- κ dielectrics and maintaining moderate band gaps in the 0.9- to 1.2-eV range down to monolayer thickness.

Two-dimensional semiconductors have attracted much attention, with subnanometer-thin single layers (1L) enabling nanoscale transistors and a lack of dangling bonds avoiding surface roughness scattering, which dominates in ultrathin silicon films (6–9). These 2D materials have nonetheless introduced new challenges, such as a larger electronic gap (of the order of 2 eV in single-layer WSe₂, MoS₂, and black phosphorus) (10, 11) and non-negligible contact resistance (8) increasing the voltage required for device operation. Moreover, high- κ gate insulators (for example, HfO₂, ZrO₂, and Al₂O₃) cannot be easily integrated with most 2D materials because of the aforementioned chemically inert surfaces free of dangling bonds (6, 12). Proposed solutions include evaporated metal-oxide buffers (13) and ozone or O₂ plasma treatments to create nucleation sites for further oxide growth by atomic layer deposition (ALD) (12, 14–17). However, this interfacial engineering perpetuates a long-standing flaw in high- κ integration on silicon, wherein several angstroms of native SiO_x are grown as a buffer, deteriorating the series capacitance of the combined dielectric gate stack (4, 5). In addition, for Mo- and W-based dichalcogenides, this approach is nonideal because MoO₃ and WO₃, respectively, are not good insulators and may even act as dopants (15, 17, 18).

Here, we focus on the layered diselenides HfSe₂ and ZrSe₂ (19–23), motivated by their moderate band gap (0.9 to 1.1 eV in bulk) (22, 24) and their possibility of forming native HfO₂ and ZrO₂ high- κ dielectrics (24). This was recently observed for HfS₂, which is a material with wider bulk gap of ~2 eV (25, 26). We first elucidate the electronic structure for both semiconductors, combining measurements by angle-resolved photoemission spectroscopy (ARPES) and computational projections, which reveal minimal band gap renormalization down to single layer thickness. Cross-sectional electron microscopy provides insight into the formation of the high- κ oxides, which had previously limited device studies to bulk (10 to 20 nm thick) HfSe₂ transistors with low current densities (27–29). We achieve air-stable devices by an entirely air-free fabrication scheme using nitrogen gloveboxes, vacuum transfer chambers, and protective encapsulation layers. Transistors down to three-layer (3L) thickness display low hysteresis, on/off current ratio of >10⁶, and current density up to ~30 μ A/ μ m. We also uncover the advantages of pairing these materials with their

Copyright © 2017
The Authors, some
rights reserved;
exclusive licensee
American Association
for the Advancement
of Science. No claim to
original U.S. Government
Works. Distributed
under a Creative
Commons Attribution
NonCommercial
License 4.0 (CC BY-NC).

¹Department of Electrical Engineering, Stanford University, Stanford, CA 94305, USA.

²Department of Physics, Stanford University, Stanford, CA 94305, USA. ³Stanford Institute for Materials and Energy Sciences, Stanford Linear Accelerator Center National Accelerator Laboratory, Menlo Park, CA 94025, USA. ⁴Department of Materials Science and Engineering, Stanford University, Stanford, CA 94305, USA.

⁵Department of Applied Physics, Stanford University, Stanford, CA 94305, USA. ⁶Precourt Institute for Energy, Stanford University, Stanford, CA 94305, USA.

*Present address: College of Optoelectronic Science and Engineering, National University of Defense Technology, Changsha 410073, China.

†Corresponding author. Email: epop@stanford.edu

native high- κ oxides, which suppress the thermal activation of interfacial trap states.

RESULTS

Electronic band structure

We synthesized bulk crystals of HfSe₂ and ZrSe₂ from elemental precursors by chemical vapor transport (CVT) using iodine as a transport agent (see Materials and Methods) (19, 30). Both compounds crystallize in the CdI₂ (1T) polytype with octahedral metal coordination, resembling the MoS₂ structure but with top and bottom rows of chalcogen atoms staggered relative to one another (Fig. 1A). Synthetic diselenide crystals have been previously characterized as n-type semiconductors, with optical absorption (19, 20, 23), ARPES (22), and scanning tunneling spectroscopy (STS) (24) measurements establishing indirect band gaps of ~1.1 to 1.2 eV for bulk HfSe₂ and ZrSe₂, respectively. The STS measurements also revealed a ~4.0-eV electron affinity χ for HfSe₂ (24), analogous to bulk Si, $\chi = 4.05$ eV (31).

We performed ARPES on vacuum-cleaved, centimeter-scale crystals, initially mapping Fermi levels $E_F \sim 1.0$ to 1.2 eV above valence band maxima (VBM) at the central Γ point (see fig. S1), matching similar reports for molecular beam epitaxy-grown, undoped 3L-ZrSe₂ and six-layer (6L)-HfSe₂ (32, 33). In situ electron doping via sodium evaporation raised E_F by ~100 meV, revealing features that correspond to conduction band minima (CBM) at the six shared M points of the reciprocal cell in both materials (Fig. 1, B and C). Indirect band gaps $E_{\Gamma-M} \approx 1.07$ eV (1.30 eV) were extracted for bulk ZrSe₂ (HfSe₂), slightly exceeding theoretical values of 1.02 eV (1.18 eV) from density functional theory (DFT) superimposed as lines in Fig. 1 (see section S1 for details). The hybrid density functional (HSE06) (34) used in the present DFT calculations correctly describes the band gap of both ZrSe₂ and HfSe₂ and agrees in fine detail with the experimental measurements, including valence sub-band structure (see further discussion in section S1, including recent underestimates of this gap by other DFT techniques). Full band structure calculations (fig. S2) project slightly smaller gaps between Γ and L , the cross-plane analog of the M point in the reciprocal lattice, representing a more 3D bulk electronic dispersion than that of Mo- or W-based 2D semiconductors

(albeit one previously proposed in corrections to structural models for ZrSe₂) (22, 35). Although not measurable in our ARPES configuration, bulk values of $E_{\Gamma-L} \approx 0.84$ eV (1.02 eV) are calculated for ZrSe₂ (HfSe₂). The latter emerges as a strong candidate for the 1.13-eV energy gap of 10L-thick HfSe₂ revealed by STS measurements (24), given the magnitude of our other underestimates. Our calculations also project minimal renormalization of electronic gap down to single layer (fig. S2), with the disappearance of interlayer L points and a lowering of CBM at M producing $E_G = E_{\Gamma-M} \approx 0.95$ eV (1L-ZrSe₂) and 1.13 eV (1L-HfSe₂).

This minor band gap renormalization relative to MoS₂ and other 2D semiconductors is partially attributed to the 1T crystal structure resulting in conduction band L valleys sitting energetically below those at M points (see fig. S2 for experimental 1T structure contrasted with fig. S3 for a hypothetical 2H structure). Sample thinning would raise the energy of L minima while lowering those of M , with the former no longer present in isolated monolayers. Moderate, indirect band gaps from ~0.9 to 1.2 eV are thus expected to persist from bulk to single layer in these selenides, which bodes well for low-voltage operation requirements in nanoscale transistors.

Ambient oxidation and air-free fabrication

To understand the process of HfSe₂ and ZrSe₂ oxidation (24, 27), we turn to cross-sectional transmission electron microscopy (TEM) in Fig. 2 (see Materials and Methods). Multilayer samples were exfoliated onto Si in an inert environment [nitrogen glovebox, O₂ and H₂O < 1 parts per million (ppm)], solvent-cleaned, and left exposed to open laboratory air for variable time intervals. Figure 2A presents cross sections for a smaller ZrSe₂ flake (~50 nm thick, <10 μ m in size) after 3 days of exposure, and Fig. 2B examines a larger, thicker (>120 nm) HfSe₂ flake after 7 days. High-resolution imaging of the former sample reveals growth of an amorphous oxide, primarily from the top-down but also with a smaller bottom interface component (from lateral diffusion of oxygen and moisture). Energy-dispersive x-ray (EDX) mapping of elemental lines indicates clear displacement of Se by O in structurally amorphous regions, relative to the layered bulk, whereas constant metal concentrations throughout suggest formation of sub-stoichiometric ZrO_{*x*}.

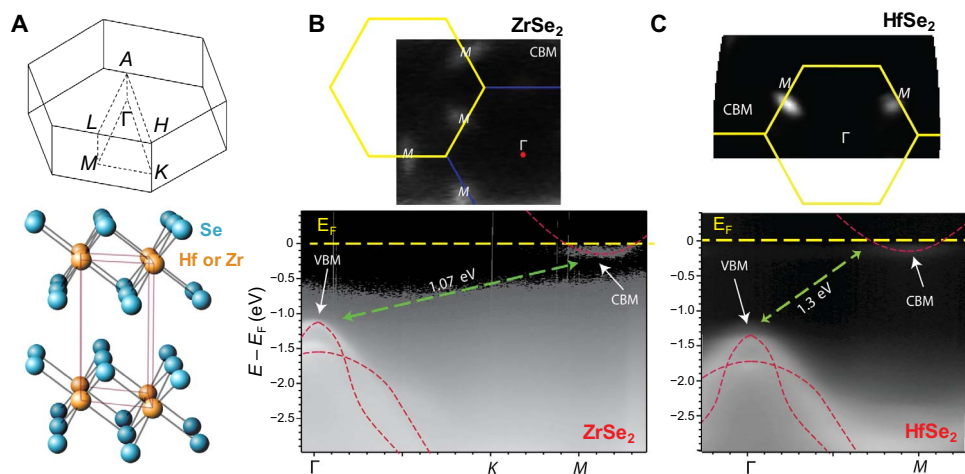


Fig. 1. Physical and electronic structure. (A) Crystal structure of HfSe₂ and ZrSe₂ along with reciprocal unit cell (top) outlining high-symmetry points. In-plane ARPES spectra of in situ vacuum-cleaved, Na doped (B) ZrSe₂ and (C) HfSe₂ reveal a band structure around the VBM (at Γ point) and lower edges of CBM (at M point), along with reciprocal space distributions of degenerate CBM valleys. Dashed red lines are the theoretical band structure from DFT calculations (HSE06 hybrid functional) in the Γ to M direction, adjusted for a ~0.05-eV (~0.12 eV) underestimate for Γ to M energy gaps of ZrSe₂ (HfSe₂).

For the larger HfSe₂ sample in Fig. 2B, a pristine bottom interface is obtained against a thin buffer of native SiO₂, despite longer exposure times producing a thicker amorphous HfO_x top film. These experiments suggest that ambient oxidation is not self-limiting for our layered selenides, ostensibly aided by oxygen diffusion through atomic-scale imperfections, such as Se vacancies. Simultaneous top and bottom growth of amorphous metal oxides is comparable to that observed in few-layer metallic 1T-TaS₂ by analogous FIB (focused ion beam) and TEM imaging (36). We estimate initial ambient oxidation rates of 5 to 10 nm per day for our large-area, bulk samples, depending on the degree of volumetric expansion during this process (25), and gradually declining over time as access is restricted to buried layers. Oxidation rates may increase from lateral diffusion of oxygen and moisture on smaller, few-layer samples and are further accelerated by open-air processing and any heating. These technologically relevant oxides present novel opportunities for high- κ dielectric integration, as readily observed by laser heating oxidation of ZrSe₂ crystals directly into tetragonal and monoclinic ZrO₂ (fig. S4).

Figure 3A shows the schematic of a completed few-layer HfSe₂ or ZrSe₂ transistor. To limit the ambient oxidation of these materials and obtain stable few-layer devices, we developed a completely air-free fabrication scheme in which material surfaces are exposed only to inert atmospheres (multiple nitrogen gloveboxes, O₂ and H₂O < 3 ppm) or vacuum chambers throughout processing. In situ glovebox capabilities included electron beam (e-beam) resist spinning/baking and ALD of multiple dielectrics, facilitating protective encapsulation before transfer to external lithography and probing tools (see Materials and Methods). HfSe₂ and ZrSe₂ flakes were exfoliated onto 90-nm SiO₂ on p⁺ Si substrates in a N₂ atmosphere and immediately capped with a 25 Å film of amorphous AlO_x by low-temperature ALD [alternating trimethylaluminum (TMA) and H₂O pulses at 150°C] loaded directly from the glovebox. This thin dielectric plays a dual role, both as a protective encapsulation layer against trace oxygen or moisture (as recently applied for air-stable capping of WTe₂) (37) and as a thin tunnel barrier for charge injection in metal-interlayer-semiconductor (MIS) contacts (Fig. 3A). MIS contacts use an ultrathin interlayer to separate metals from semiconductors, preventing Fermi level pinning in the semiconductor band gap (38). The 25 Å AlO_x barrier provided optimum yield of transistors, and comparable MIS layers have led to

improvements in contact resistance R_C for MoS₂ with Al-, Ta-, and Ti-metal oxides (39, 40).

These capped flakes were coated with 300-nm poly(methyl methacrylate) (PMMA; N₂ atmosphere), providing temporary encapsulation while serving as e-beam resist for local marker and contact patterning. Resist development was followed by vacuum chamber transfer into a metal evaporator (see Materials and Methods), depositing Cr/Au contacts (15/45 nm). Ti/Au, Pd, Ag, and pure Au contacts were also evaluated, spanning a work function range of ~1 eV, but achieved significantly worse n-type performance. After metal lift-off in the original glovebox, the interfaced ALD chamber was used to enclose devices within a further 200 Å of AlO_x, serving as an oxygen and moisture barrier during transfer to a vacuum probe station in which a final 1-hour 250°C anneal was performed.

Compatibility of exfoliated samples with high- κ dielectrics was evidenced by the uniform nucleation of AlO_x capping layers, which were free of pinholes and of equivalent roughness (root mean square, ~0.35 nm) both on and off flake surfaces under atomic force microscopy (AFM) topographic mapping. Smooth oxide coverage enabled direct layer counting from AFM height profiles, correlating flake thickness to approximate integer multiples of the interlayer spacing of HfSe₂ and ZrSe₂ (both ~0.62 nm) (19, 20).

Figure 3B shows a cross-sectional TEM image from the channel of an eight-layer (8L) HfSe₂ device (confirming its AFM thickness) with outlines of the first seven layers clearly visible and partial signs of an eighth layer blending into the top AlO_x film. Its consumption by the top dielectric suggests partial oxidation during fabrication, despite extensive efforts to limit trace oxygen and moisture, carefully seeding ALD at reduced temperatures (see Materials and Methods). TEM cross sections at device contacts (fig. S6) show similar features, with discernable outlines of a broadened top layer contributing up to ~5 Å to the ~25 Å MIS oxide (consistent with reports of 250% cross-plane volumetric expansion in oxidized HfS₂, as well as increased thickness for O₂ plasma-exposed HfSe₂) (25, 29). TEM profiles qualitatively resemble those of HfO_x on partially oxidized WSe₂ top layers, following “self-cleaning” ALD reactions reducing a surface WO_x layer formed by ozone exposure (16). However, a fortuitous native HfO_x layer presents clear benefits for gate integration compared to trace metallic W or Mo (or their conductive oxides in the absence of self-cleaning reduction).

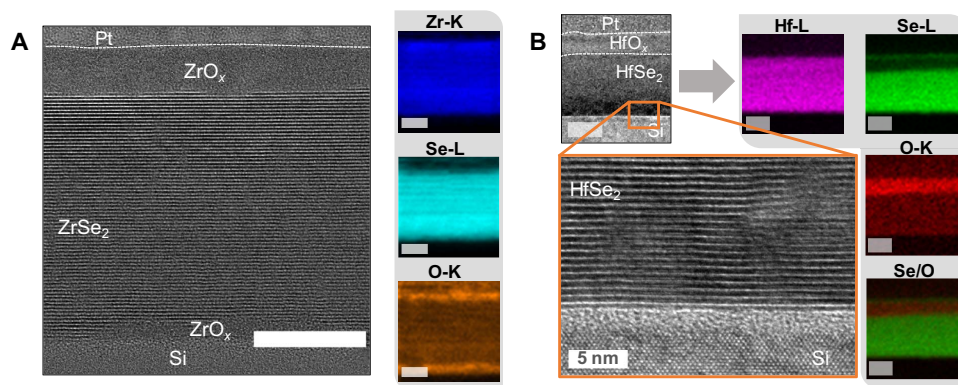


Fig. 2. Cross-sectional TEM and EDX mapping of native oxide formation. (A) Cross-sectional TEM image of a smaller (<50 nm thick, <10 μm in lateral size) ZrSe₂ flake following 3 days of ambient exposure, demonstrating both top-down and bottom-up oxidation into amorphous ZrO_x, which partially consumes individual layers. Insets show that EDX elemental mapping demonstrates displacement of Se by O in oxidized regions. Scale bars, 20 nm. (B) Similar TEM images of a larger (>100 μm), thicker HfSe₂ flake after 7 days of ambient exposure, with greater extent of top-down oxidation into HfO_x, despite a pristine bottom interface with the Si substrate. Insets show EDX elemental mapping confirming complete chalcogen depletion, illustrated via overlay of O and Se signals. Scale bars, 50 nm.

This incidental oxidation may explain the lack of measurable charge transport in samples thinner than 3L (~ 1.8 nm), alongside strong reduction of optical contrast for bilayer flakes, suggesting complete consumption. The proximity of an oxidized layer to a 2D electron gas (2DEG) holds several implications to subsequent discussions of trap states and interfacial engineering. Samples are hereafter referred to by AFM-assigned layer counts (for example, 3L or 8L), although it is likely that the topmost layer(s) do not contribute to charge transport because of partial oxidation.

Encapsulated device characterization

Figure 3 (C and D) shows current versus gate voltage (I_D versus V_{GS}) measurements of few-layer HfSe₂ transistors, modulated using the back gate shown in Fig. 3A. Samples between 3 and 13 layers thick (~ 1.8 to 8.1 nm) were probed under vacuum, with channel length varying from $L = 90$ nm to $L = 2.5$ μm . Devices of all thicknesses demonstrated clear turn-off, with on/off current ratios of $\sim 10^6$ at 300 K for source-drain bias $V_{DS} = 1$ V (approaching 10^7 for thicker samples cooled to 200 K). As marked by the arrows, all data shown are double sweeps around back-gate $V_{GS} = 0$ V, revealing relatively low hysteresis consistent with previous reports for vacuum-annealed 2D transistors under AlO_x encapsulation (41). Current densities of shortest devices (90 to 150 nm) reached 25 to 30 $\mu\text{A}/\mu\text{m}$ (Fig. 3C, inset), although super-linear dependence on V_{DS} suggests contact-limited behavior. These current densities represent two orders of magnitude improvement over previous reports in substantially thicker HfS₂ and HfSe₂ devices at comparable biasing (25, 27–29). Inverse subthreshold slope (SS) of 3.2 to 4.2 V per decade is found on the 90-nm SiO₂ back-gate oxide, although SS is likely limited by the relatively thick tunnel barriers at our unoptimized MIS contacts. Similar SS values were reported for few-layer MoS₂ on comparable back gates, with larger Schottky barriers to the conduction band (42).

Room temperature field-effect electron mobilities $\mu_{FE} = 1$ to 4 $\text{cm}^2 \text{V}^{-1} \text{s}^{-1}$ (Fig. 3D, inset) are extracted as $\mu_{FE} = L/(C_{ox} V_{DS} W)(dI_D/dV_{GS})$, where W is the channel width and $C_{ox} \approx 38 \text{ nF}/\text{cm}^2$ is the capacitance of the SiO₂. Mobility values are modestly improved (by a factor of ~ 2 to $5\times$) when accounting for contact resistance via transfer length mea-

surement (TLM) analysis on devices with multiple channel lengths (fig. S7), revealing non-negligible $R_C \approx 50$ to 100 kilohms- μm . This contact resistance is two orders of magnitude greater than that of the best MoS₂ devices (8) but is not unexpected for the unoptimized MIS contacts used here, with possible material degradation at exposed contact regions during partial vacuum transfer to an external metallization tool. We note that the mobility estimate is complicated here by temperature-dependent shifts of the threshold voltage, as described below. Chemical stability of the alumina capping layer resulted in minute (few percentages) degradation of device currents after 1 to 2 months of storage in nitrogen ambient, with comparably stable hysteresis and threshold voltage. Open-air aging of devices (fig. S5) indicates that this encapsulation provides several weeks of ambient stability.

Figure 4 shows qualitatively similar trends for AlO_x-capped ZrSe₂ devices with identical MIS contacts, albeit with lower mobilities (relative to our HfSe₂) despite smaller projected semiconducting band gaps, $E_G = 0.84$ eV. Air-stable encapsulation of films from 3L to bulk enabled Raman spectroscopy of characteristic phonon modes (Fig. 4A), comparable to reported values of cross-plane A_{1g} (193 cm^{-1}) and in-plane E_g (145 cm^{-1}) peaks (43). These modes shift very little ($<1 \text{ cm}^{-1}$) as film thickness is reduced compared to other dichalcogenide crystals (6). Transistor transfer curves show current densities approaching 20 $\mu\text{A}/\mu\text{m}$ (Fig. 4B) and on/off ratios of 10^5 to 10^6 for 5L- to 6L-thick devices with submicrometer channel lengths (Fig. 4C), achieving room temperature $\mu_{FE} = 1$ to 1.5 $\text{cm}^2 \text{V}^{-1} \text{s}^{-1}$. The thinnest working devices were again 3L, although these demonstrated reduced drive currents ($I_D \approx 0.1 \mu\text{A}/\mu\text{m}$ and $I_{ON}/I_{OFF} \approx 10^5$ for $L = 0.52 \mu\text{m}$) and contact-limited mobility ($0.1 \text{ cm}^2 \text{V}^{-1} \text{s}^{-1}$) relative to channels thicker than 5L. Sensitivity to material degradation may be more acute for ZrSe₂, although no outward signs of oxidation or poor dielectric coverage were found in scanning electron microscopy (SEM) analysis (Fig. 4, C and D, insets). Cooling to 80 K revealed improved on/off current ratios across all devices, to $\sim 10^7$ for the 6L sample in Fig. 4D, alongside forward shifts in threshold voltage V_T resembling those of AlO_x-capped HfSe₂ devices in Fig. 3D. Subthreshold swing nearly halves from 3.5 V per decade at room temperature to 1.5 to 2 V per decade below 150 K.

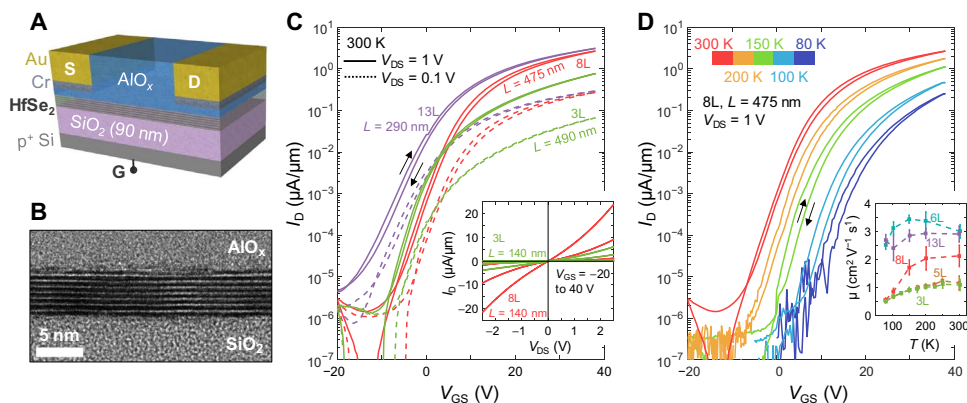


Fig. 3. HfSe₂ transistors. (A) Schematic of HfSe₂ device, back-gated through 90-nm SiO₂, and with ALD alumina used as both protective encapsulation and a ~ 25 Å interlayer in an MIS contact scheme (contact layers not to scale; capping alumina over contact metals not shown). (B) High-resolution TEM image of the channel of an 8L-thick HfSe₂ device, with evidence of a partially oxidized top layer integrated into the capping oxide. (C) Room temperature transfer curves of HfSe₂ transistors with varying channel thickness, demonstrating an on/off current ratio of $\sim 10^6$ at $V_{DS} = 1$ V. Inset: Linear I_D versus V_{GS} plots for short-channel devices ($L \approx 140$ nm) with 3L and 8L channels. All curves are dual sweeps from the origin, demonstrating low hysteresis (see arrows). (D) Temperature dependence of transfer curves for the 8L-thick HfSe₂ device, from 80 to 300 K. The threshold voltage shifts higher as the sample is cooled. Inset: Field-effect mobilities of encapsulated 3L to 13L (~ 1.8 to 8.1 nm thick) HfSe₂ devices.

Understanding the interfaces

The negative shift of threshold voltage observed with increasing temperatures (Figs. 3D and 4D) has precedent in 2D electron systems; it has been examined in heterostructure field-effect transistors [HFETs; alternatively labeled high-electron mobility transistors (HEMTs)] formed by confined 2DEGs near conduction band offsets at junctions such as AlGaIn/GaN (44–46). This phenomenon is particularly prominent in AlGaIn/GaN and InAlN/GaN devices with Al₂O₃ top-gate dielectrics, where it was attributed to thermal activation of charge traps at defect sites in imperfect semiconductor-oxide interfaces (45, 46). Negative V_T shifts with elevated temperature are triggered by donor states deep (~200 meV) within the band gap, contributing free carriers despite a spatial offset of several nanometers between the oxide interface and the buried 2DEG. This is facilitated by the polarity of the channel material, a common property of III-V compounds and of layered Hf- and Zr-based dichalcogenides (6, 21).

The interface of our oxidized top channel layer appears to play a similar role to the oxide-nitride cap interface in HEMTs. Our MIS contact scheme allows substitution of different thin “I” layers while retaining air-stable encapsulation with a global 20-nm alumina. We evaluated two configurations across multiple HfSe₂ devices 3L to 8L thick, using 25 Å layers of AlO_x and HfO_x (Fig. 5A) deposited immediately after exfoliation in a glovebox ALD system at 150°C. For AlO_x interlayers, the general trends of Figs. 3D and 4D are replicated in back-gate sweeps across all channel thicknesses; average threshold voltage shifts ΔV_T of 10 to 15 V are recorded while cooling from 300 to 80 K in Fig. 5B (blue data points).

This consistent temperature dependence of V_T enables estimates of trap density N_{IT} from a simplified HFET charge-neutrality model (45), $N_{IT} = \Delta V_T(2C/q)$. Here, C is the net capacitance per area, calculated from the series combination of C_{ox} and a finite semiconductor depth (C_s with $\kappa_{\text{HfSe}_2} = 8.05$) (47), assuming a 2DEG peaked at the center of flake thickness (48). Despite a lower gate capacitance than that of conventional HFETs, dominated by the single back gate across all sample thicknesses, a range of $N_{IT} = 3 \times 10^{12}$ to 8×10^{12} cm⁻² for the HfSe₂/HfO_x/AlO_x stack mirrors the 2.5×10^{12} to 7.5×10^{12} cm⁻² estimated for MoS₂/AlO_x top-gate interfaces via hysteresis, SS, and charge collection spectroscopy (49, 50). Figure 5C shows an Arrhenius analysis of the trap thermal response, fitting an exponential evolu-

tion of density N_{IT} with temperature by an activation energy $E_A \approx 26$ to 32 meV comparable to the Boltzmann energy at room temperature. The characteristic shift in transfer curves for AlO_x interlayers is thus associated with a high density of relatively shallow trap states, which activate on an energy scale corresponding to heating from 80 K to ambient.

Devices with HfO_x MIS contacts (orange data points in Fig. 5B) have smaller threshold shifts down to 80 K, lacking the monotonic increase seen in all AlO_x samples. This can also be seen by comparing the inset of Fig. 5B (hafnia interface to HfSe₂) with Figs. 3D and 4D (alumina interface). In other words, the transfer curves at 80 and 300 K are nearly the same, except for the sharper turn-on at the lower temperature. Device on/off ratio, subthreshold swing, and mobility remain similar to those with all AlO_x encapsulation (Fig. 3), despite slight widening of the hysteresis envelope (from ~1 to ~2 V across a 60 V sweep). The choice of an HfO_x interlayer, nominally the native oxide of the constituent transition metal, thus offers measurable improvement of the interfacial quality. Further studies are needed to develop a mechanistic understanding of this phenomenon, that is, whether it is grounded in a fundamental material compatibility between ALD oxides and self-limiting, oxidized diselenide layers, or it is a consequence of the difference in material dielectric constant ($\kappa_{\text{HfO}_x} \approx 2\kappa_{\text{AlO}_x}$). Regarding the former hypothesis, the oxidized top HfSe₂ layer may be best passivated by ALD of the same metal oxide, potentially driving more complete oxidation of this layer. Less reactive AlO_x growth may produce an inconsistent AlO_x/HfSe_{2-y}O_y interface, containing the traps quantified in Fig. 5C.

Top-gated transistors with native high- κ oxides

To exploit the native integration of HfO₂ with HfSe₂, we fabricated the first top-gated transistors of this kind, as shown in Fig. 6. These devices include the 2.5-nm MIS contacts discussed earlier and a further 17-nm layer of HfO₂ deposited by ALD [with a total equivalent oxide thickness (EOT) ≈ 4.75 nm]. A Cr/Ag metal gate is patterned by a negative-tone resist process, protecting channel regions by low-energy metal deposition and no direct exposure to e-beam patterning (see Materials and Methods). Figure 6 shows the current versus top-gate voltage of such a transistor with 7L channel thickness and ~1 μm channel length (the gate length is slightly larger, overlapping the contacts). DC sweeps

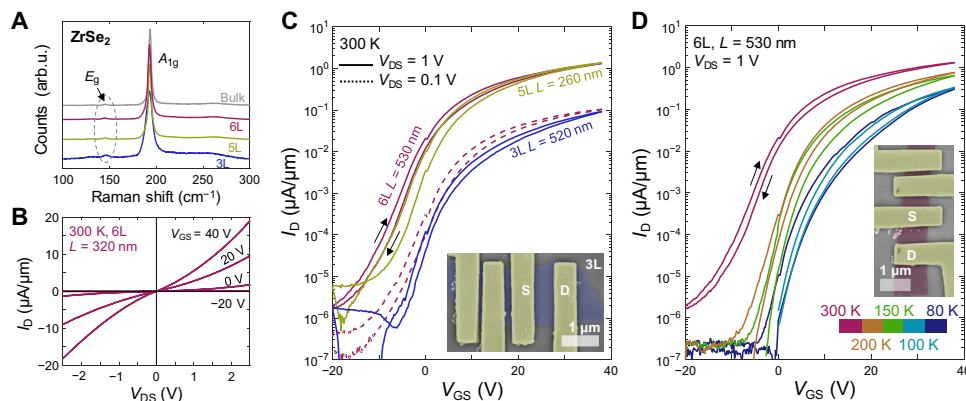


Fig. 4. ZrSe₂ transistors. (A) Low-power Raman spectra of ZrSe₂ devices encapsulated by AlO_x from 3L to bulk, with minute shifts of A_{1g} (~193 cm⁻¹) and E_g (~145 cm⁻¹) modes as the thickness is reduced (532 nm laser). arb.u., arbitrary units. (B) Hysteresis-free room temperature I_D versus V_{DS} forward and reverse sweeps for a 6L-thick ZrSe₂ transistor ($L = 320$ nm) with a current density up to ~20 $\mu\text{A}/\mu\text{m}$. (C) Transfer curves of back-gated ZrSe₂ transistors of varying channel thickness show lower current density in the thinnest (3L) devices. (D) Temperature-dependent transfer curves of the 6L device between 80 and 300 K show improved on/off current ratios with cooling (approaching 10^7) and forward shift in threshold voltage at lower temperatures. Insets are false-colored SEM micrographs of 3L and 6L devices, with source (S) and drain (D) contacts as labeled.

starting at $V_{GS} = 0$ (solid black curve) manifest current modulation up to 10^6 , with hysteresis and nonideal SS (200 to 350 mV per decade) indicative of charge trapping (49).

Nonetheless, most charge trapping effects can be bypassed with pulsed measurements (red dashed lines in Fig. 6) using pulse widths shorter than average charge trapping time constants. Using 125 μ s wide V_{GS} pulses with 10 μ s rise and fall time drastically reduces the hysteresis and enhances current density to values comparable with our previous back-gated transistors. The contact-limited field-effect mobility is ~ 0.3 $\text{cm}^2 \text{V}^{-1} \text{s}^{-1}$, lower than in back-gated devices ostensibly because of scattering at the top interface with the partially oxidized layer and lack of gating under contact regions. We note that top-gated transistors

are more sensitive to interfacial traps than back-gated devices, given that current flow is concentrated at the top HfSe₂ interface (versus the middle or bottom interface in back-gated devices) (48). These results further emphasize the continued need to study high-quality native oxide formation in these top-gated transistors.

DISCUSSION

Several discoveries made in the course of this work suggest advantages of both HfSe₂ and ZrSe₂ for 2D electronics. First, unlike MoS₂ or black phosphorus, the band gap of these selenides appears to change very little as the material thickness is scaled from bulk to single layers, remaining indirect and in the 0.9- to 1.2-eV range. This invariance is likely to enable higher tolerance for variability in system-level applications because large-area growths could yield a combination of single- and few-layer regions (6). Second, the band gap is comparable to that of silicon, small enough to allow low-voltage operation of future electronics but large enough to enable $>10^6$ on/off current ratios, along with the benefits of 2D materials (namely, an atomically thin body for ultrascaled transistors). In contrast, most other 2D semiconductors have larger band gaps around 2 eV or higher in single layers.

Third, HfSe₂ and ZrSe₂ benefit from native oxides HfO₂ and ZrO₂, a property similar to that of silicon, but with technologically more desirable high- κ insulators. This behavior is rare among known semiconductors because desirable oxides form neither on Ge and III-V compounds, nor on other moderate-gap 2D semiconductors. Thus, results shown here represent the first demonstration of 2D transistors with native high- κ oxides, although further work is needed to improve the quality of the interfaces obtained. A fourth advance made in this work is the air-free processing of these materials with standard microfabrication techniques, which has enabled our study of thinner samples (down to 3L) with higher current densities (up to ~ 30 $\mu\text{A}/\mu\text{m}$) than has been achieved even on bulk samples with these materials.

Transistor performance may be improved with refined processing, engineering contacts and interfaces toward enhanced current densities and intrinsic mobility. We note that, even in air-stable MoS₂, existing measurements record several orders of magnitude variation in these parameters, depending on contact and channel processing, as well as top/bottom interfaces (including mitigating effects of substrate roughness, adsorbates, and charge traps by encapsulation in insulating van der Waals heterostructures) (51, 52). Across our yet unoptimized devices, imperfect MIS contacts with relatively thick "P" barriers could be avoided by development and metallization in an entirely enclosed, inert atmosphere. Threshold voltage shifts also appear to be induced by shallow interfacial trap states, highlighting novel challenges of interfacial engineering for layered materials with native oxides formed during processing. Selective oxidation of only the topmost layer(s) would enable improved growth of desirable high- κ dielectrics, for example, by controlled, layer-selective oxidation with pulsed ozone or oxygen plasma recently applied to other 2D materials (12, 15, 17).

CONCLUSIONS

In summary, we performed a systematic evaluation of HfSe₂ and ZrSe₂, layered 2D materials with native high- κ dielectrics, demonstrating the first such electronic devices with few-layer channels. Computational and ARPES studies reveal minimal change of electronic band gap with decreasing layer number, whereas TEM characterization identified the formation of amorphous native oxides. Stable devices, fabricated under

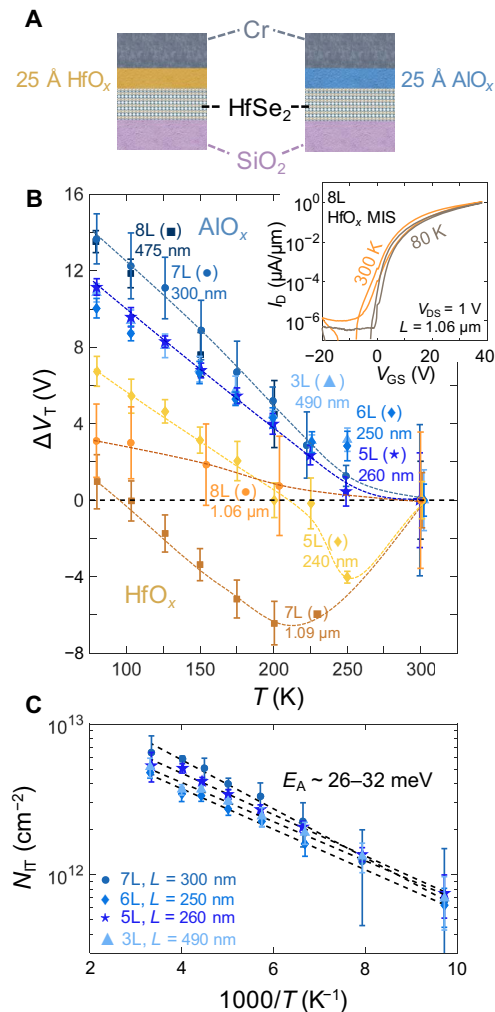


Fig. 5. Interfacial oxide engineering. (A) Configuration of MIS contacts for HfSe₂ transistors with 25 Å interlayers of either AlO_x or HfO_x ALD oxide (global 200 Å alumina capping is used for both). (B) Mean shift in threshold voltage ΔV_T from the 300 K baseline for multiple HfSe₂ devices cooled to ~ 80 K, contrasting the effects of AlO_x (blue) and HfO_x (orange) interlayers. V_T was extracted from the linear intercept at the point of peak transconductance. Dashed lines are guides to the eye. Inset shows transfer characteristics of an 8L-thick HfSe₂ device with HfO_x interlayer at 80 and 300 K, demonstrating a minimal shift of V_T and steeper turn-on behavior at lower temperatures. (C) Temperature evolution of estimated interfacial trap density N_{IT} for multiple HfSe₂ devices with AlO_x interlayers, as calculated from ΔV_T (see text). Dashed lines are fits to Arrhenius activation energies of 26 to 32 meV.

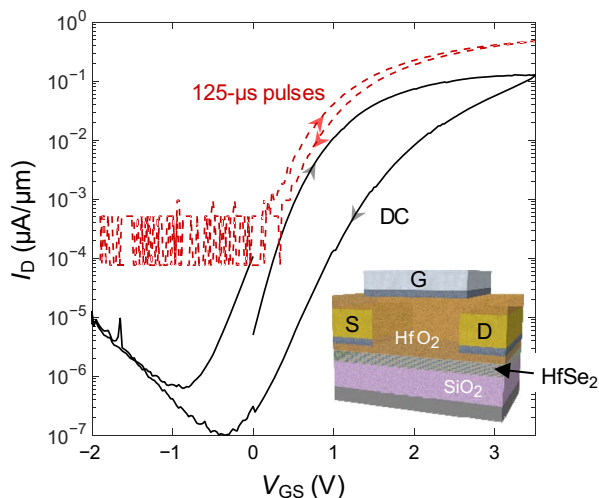


Fig. 6. Top-gated HfSe₂ transistor with native HfO₂ dielectric. Measured transfer characteristics of a top-gated 7L-thick HfSe₂ transistor with 2.5-nm HfO_x MIS contacts and 19.5-nm HfO₂ top-gated dielectric (EOT ≈ 4.75 nm). The channel length is $L \approx 1 \mu\text{m}$, $V_{DS} = 1 \text{ V}$, and $T = 295 \text{ K}$, and the Si substrate was grounded. DC measurements (solid black lines) reveal $\sim 10^6$ on/off current ratio, despite noticeable hysteresis and SS of ~ 200 to 350 mV per decade. Pulsed measurements (dashed red lines, with 125 μs pulse width and 10 μs fall/rise times) reduce the hysteresis and achieve higher current density, although the low-current resolution is limited. Inset shows device schematic with source (S), drain (D), and gate (G) electrodes as labeled.

inert atmospheres, demonstrated multiple orders of magnitude improvement in current density for these materials relative to bulk studies (27–29). We also conducted a preliminary study of interfacial trap states and their suppression through the choice of compatible dielectrics. Both HfSe₂ and ZrSe₂ have moderate band gaps, regardless of layer number, and readily form native high- κ oxides, reproducing for the first time two key attributes of silicon for large-scale technological integration in a 2D nanomaterial, intrinsically scalable to the atomically thin limit.

MATERIALS AND METHODS

Crystal growth

Bulk crystals of HfSe₂ and ZrSe₂ were grown by CVT from stoichiometric mixtures of elemental Hf powder (Alfa Aesar, 99.6%), Zr slugs (Alfa Aesar, 99.95%), and Se powder (Alfa Aesar, 99.999%). These were sealed in quartz tubes evacuated under argon, with iodine (Alfa Aesar, 99.99+%) added at 5 mg/cm^3 as a transport agent. Growth took place for 14 days along an 11-cm transport length, corresponding to a $\sim 100^\circ\text{C}$ thermal gradient in a single-zone furnace with central temperatures of 900° or 950°C . Both temperatures produced large amounts of platelet-like crystals with facets several millimeters to $>1 \text{ cm}$ in size. ZrSe₂ crystals were uniformly dark green, whereas those of HfSe₂ were metallic gray.

ARPES measurements

ARPES measurements were performed at Beamline 10.0.1.1 of the Advanced Light Source of Lawrence Berkeley National Laboratory. Bulk crystals were cleaved in situ at 10 K in ultrahigh vacuum. Sodium was evaporated onto the cleaved sample surface in situ, with pressure less than 10^{-10} torr during evaporation. All data were collected using 75 eV photons. ARPES measurements were carried out with a total energy resolution of $\sim 25 \text{ meV}$ and base pressures below 5×10^{-11} torr.

DFT calculations

DFT calculations were performed using the hybrid density functional HSE06, as implemented in the Vienna Ab initio simulation package (34). In the HSE06 functional, 25% of the short-range exchange interaction of the Perdew-Burke-Ernzerhof generalized gradient approximation was replaced by the short-range nonlocal Hartree-Fock exchange interaction (34). For this study, an exchange-screening parameter ω of 0.2 \AA^{-1} was applied for both HfSe₂ and ZrSe₂. All calculations were performed using the projector augmented wave method; Zr (4s, 4p, 5s, and 4d), Hf (5p, 6s, and 5d), and Se (4s and 4p) were used as valence electron states, and spin-orbit coupling was included in the calculations. Bulk ($8 \times 8 \times 8$) and monolayer ($8 \times 8 \times 1$) Γ -centered k -point grids were used, with structures optimized for lattice constants and internal ionic coordinates until the residual forces were less than 0.01 eV/\AA .

Device fabrication and characterization

Flakes of Hf/ZrSe₂ were exfoliated onto 90-nm SiO₂ on p⁺ Si substrates in a nitrogen atmosphere (glovebox; O₂ and H₂O < 3 ppm) using a low-residue thermal release tape (Nitto-Denko Revalpha) and cleaned with an acetone/2-propanol soak. AlO_x or HfO_x (25 \AA) interlayers were deposited in situ within an interfaced Cambridge Savannah Thermal ALD chamber [150°C , alternating H₂O and TMA or tetrakis(dimethylamido)hafnium pulses, after first saturating surfaces with 10 pulses of metal precursor], followed by spin coating of 300 nm PMMA e-beam resist (Microchem A5 950k). Samples were briefly removed from gloveboxes for mapping of target flakes and e-beam lithography of contacts (Raith 150, 20 kV), retaining PMMA coverage throughout. Patterned samples were developed in a N₂ glovebox and loaded into a custom, closed transfer stage that was pumped to $\sim 2 \times 10^{-5}$ torr and mounted inside a Lesker PVD 75 e-beam evaporator. Once mounted, this stage could be manually actuated to open when external chamber pressure matched that inside, thereby limiting contact of exposed flake surfaces to trace oxygen or moisture. Cr/Au (15/45 nm) contacts were deposited at base pressures of $\sim 5 \times 10^{-8}$ torr, with lift-off performed using acetone/2-propanol in the original glovebox. A further 200 \AA AlO_x capping layer was deposited (ALD, 150°C ; TMA/H₂O) before transfer to a Janis Cryogenic vacuum probe station (chamber pressure, 10^{-6} to 5×10^{-5} torr) for a final vacuum anneal (1 hour at 250°C , cooling to room temperature over several hours). Top-gated devices were fabricated in a variation of this process, depositing a 2.5-nm HfO_x interlayer and Cr/Au (15/35 nm) contacts before encapsulation with a further 17-nm HfO_x. MaN-2403 negative-tone resist (300 nm) was spun and patterned (Raith 150, 10 kV), lifting off a Cr/Ag (5/20 nm) top-gate electrode.

Electrical characterization of devices was performed in a Janis Cryogenic probe station, cooled with closed-loop liquid nitrogen, using 4225-RPM Remote Amplifier/Switch units connected to a Keithley 4200-SCS parameter analyzer. ALD-encapsulated flakes were profiled via AFM (Veeco Dimension 3100, soft-tapping mode) and Raman spectroscopy (HORIBA LabRAM, 532 nm laser source), with devices imaged by SEM (Raith 150, 5 to 10 kV). Cross sections of oxidized flakes (Fig. 2) were prepared with a FEI Helios NanoLab 600i DualBeam FIB/SEM using a lift-out method. A platinum layer was deposited onto the sample area for protection, with gallium ion milling performed right before TEM characterization. High-resolution TEM images were obtained using an aberration-corrected FEI Titan at 300 kV, with in situ EDX elemental mapping. Device cross sections (Fig. 3B and fig. S6) were prepared and imaged by Evans Analytical Group using a FEI Dual Beam FIB/SEM and FEI Tecnai TF-20 FEG/TEM at 200 kV.

SUPPLEMENTARY MATERIALS

Supplementary material for this article is available at <http://advances.sciencemag.org/cgi/content/full/3/8/e1700481/DC1>

section S1. Electronic band structure validation

section S2. Native oxide formation and passivation

section S3. Contact characterization

fig. S1. Undoped ARPES spectra of bulk crystals.

fig. S2. HSE06 DFT of monolayer and bulk band structure.

fig. S3. Gap divergence in hypothetical 2H-HfSe₂.

fig. S4. ZrSe₂ Raman laser oxidation.

fig. S5. Aging of capped ZrSe₂.

fig. S6. MIS contact TEM.

fig. S7. Contact TLM analysis.

table S1. Laser oxidation peaks.

References (53–58)

REFERENCES AND NOTES

- S. E. Thompson, R. S. Chau, T. Ghani, K. Mistry, S. Tyagi, M. T. Bohr, In search of “Forever,” continued transistor scaling one new material at a time. *IEEE Trans. Semicond. Manuf.* **18**, 26–36 (2005).
- L. Chang, D. J. Frank, R. K. Montoye, S. J. Koester, B. L. Ji, P. W. Coteau, R. H. Dennard, W. Haensch, Practical strategies for power-efficient computing technologies. *Proc. IEEE* **98**, 215–236 (2010).
- E. J. Nowak, Maintaining the benefits of CMOS scaling when scaling bogs down. *IBM J. Res. Dev.* **46**, 169–180 (2002).
- E. P. Gusev, E. Cartier, D. A. Buchanan, M. Gribelyuk, M. Copel, H. Okorn-Schmidt, C. D’Emic, Ultrathin high-K metal oxides on silicon: Processing, characterization and integration issues. *Microelectron. Eng.* **59**, 341–349 (2001).
- G. D. Wilk, R. M. Wallace, J. M. Anthony, High- κ gate dielectrics: Current status and materials properties considerations. *J. Appl. Phys.* **89**, 5243–5275 (2001).
- M. Chhowalla, H. S. Shin, G. Eda, L.-J. Li, K. P. Loh, H. Zhang, The chemistry of two-dimensional layered transition metal dichalcogenide nanosheets. *Nat. Chem.* **5**, 263–275 (2013).
- G. Fiori, F. Bonaccorso, G. Iannaccone, T. Palacios, D. Neumaier, A. Seabaugh, S. K. Banerjee, L. Colombo, Electronics based on two-dimensional materials. *Nat. Nanotechnol.* **9**, 768–779 (2014).
- C. D. English, G. Shine, V. E. Dorgan, K. C. Saraswat, E. Pop, Improved contacts to MoS₂ transistors by ultra-high vacuum metal deposition. *Nano Lett.* **16**, 3824–3830 (2016).
- K. Uchida, S.-i. Takagi, Carrier scattering induced by thickness fluctuation of silicon-on-insulator film in ultrathin-body metal-oxide-semiconductor field-effect transistors. *Appl. Phys. Lett.* **82**, 2916–2918 (2003).
- H. M. Hill, A. F. Rigosi, K. T. Rim, G. W. Flynn, T. F. Heinz, Band alignment in MoS₂/WS₂ transition metal dichalcogenide heterostructures probed by scanning tunneling microscopy and spectroscopy. *Nano Lett.* **16**, 4831–4837 (2016).
- X. Wang, A. M. Jones, K. L. Seyler, V. Tran, Y. Jia, H. Zhao, H. Wang, L. Yang, X. Xu, F. Xia, Highly anisotropic and robust excitons in monolayer black phosphorus. *Nat. Nanotechnol.* **10**, 517–521 (2015).
- A. Azcatl, S. McDonnell, K. C. Santosh, X. Peng, H. Dong, X. Qin, R. Addou, G. I. Mordí, N. Lu, J. Kim, M. J. Kim, K. Cho, R. M. Wallace, MoS₂ functionalization for ultra-thin atomic layer deposited dielectrics. *Appl. Phys. Lett.* **104**, 111601 (2014).
- X. Zou, J. Wang, C.-H. Chiu, Y. Wu, X. Xiao, C. Jiang, W.-W. Wu, L. Mai, T. Chen, J. Li, J. C. Ho, L. Liao, Interface engineering for high-performance top-gated MoS₂ field-effect transistors. *Adv. Mater.* **26**, 6255–6261 (2014).
- J. Wang, S. Li, X. Zou, J. Ho, L. Liao, X. Xiao, C. Jiang, W. Hu, J. Wang, J. Li, Integration of high- κ oxide on MoS₂ by using ozone pretreatment for high-performance MoS₂ top-gated transistor with thickness-dependent carrier scattering investigation. *Small* **11**, 5932–5938 (2015).
- H. Zhu, X. Qin, L. Cheng, A. Azcatl, J. Kim, R. M. Wallace, Remote plasma oxidation and atomic layer etching of MoS₂. *ACS Appl. Mater. Interfaces* **8**, 19119–19126 (2016).
- A. Azcatl, K. C. Santosh, X. Peng, N. Lu, S. McDonnell, X. Qin, F. de Dios, R. Addou, J. Kim, M. J. Kim, K. Cho, R. M. Wallace, HfO₂ on UV-O₃ exposed transition metal dichalcogenides: Interfacial reactions study. *2D Mater.* **2**, 014004 (2015).
- M. Yamamoto, S. Dutta, S. Aikawa, S. Nakaharai, K. Wakabayashi, M. S. Fuhrer, K. Ueno, K. Tsukagoshi, Self-limiting layer-by-layer oxidation of atomically thin WSe₂. *Nano Lett.* **15**, 2067–2073 (2015).
- L. Cai, C. J. McClellan, A. L. Koh, H. Li, E. Yalon, E. Pop, X. Zheng, Rapid flame synthesis of atomically thin MoO₃ down to monolayer thickness for effective hole doping of WSe₂. *Nano Lett.* **17**, 3854–3861 (2017).
- D. L. Greenaway, R. Nitsche, Preparation and optical properties of group IV-V₂ chalcogenides having CdI₂ structure. *J. Phys. Chem. Solids* **26**, 1445–1458 (1965).
- P. A. Lee, G. Said, R. Davis, T. H. Lim, On optical properties of some layer compounds. *J. Phys. Chem. Solids* **30**, 2719–2729 (1969).
- X.-g. Zheng, H. Kuriyaki, K. Hirakawa, Electrical anisotropy of layered compound ZrSe₂ and HfSe₂. *J. Phys. Soc. Jpn.* **58**, 622–626 (1989).
- H. E. Brauer, H. I. Starnberg, L. J. Holleboom, H. P. Hughes, The electronic-structure of ZrSe₂ and Cs_xZrSe₂ studied by angle-resolved photoelectron-spectroscopy. *J. Phys. Condens. Matter* **7**, 7741–7760 (1995).
- C. Gaiser, T. Zandt, A. Krapp, R. Serverin, C. Janowitz, R. Manzke, Band-gap engineering with Hf_xSe_{2-x}. *Phys. Rev. B* **69**, 075205 (2004).
- R. Y. Yue, A. T. Barton, H. Zhu, A. Azcatl, L. F. Pena, J. Wang, X. Peng, N. Lu, L. X. Cheng, R. Addou, S. McDonnell, L. Colombo, J. W. P. Hsu, J. Kim, M. J. Kim, R. M. Wallace, C. L. Hinkle, HfSe₂ thin films: 2D Transition metal dichalcogenides grown by molecular beam epitaxy. *ACS Nano* **9**, 474–480 (2015).
- S. H. Chae, Y. Jin, T. S. Kim, D. S. Chung, H. Na, H. Nam, H. Kim, D. J. Perello, H. Y. Jeong, T. H. Ly, Y. H. Lee, Oxidation effect in octahedral hafnium disulfide thin film. *ACS Nano* **10**, 1309–1316 (2016).
- K. Xu, Y. Huang, B. Chen, Y. Xia, W. Lei, Z. Wang, Q. Wang, F. Wang, L. Yin, J. He, Toward high-performance top-gate ultrathin HfS₂ field-effect transistors by interface engineering. *Small* **12**, 3106–3111 (2016).
- M. Kang, S. Rathi, I. Lee, D. Lim, J. Wang, L. Li, M. A. Khan, G. H. Kim, Electrical characterization of multilayer HfSe₂ field-effect transistors on SiO₂ substrate. *Appl. Phys. Lett.* **106**, 143108 (2015).
- L. Yin, K. Xu, Y. Wen, Z. Wang, Y. Huang, F. Wang, T. A. Shifa, R. Cheng, H. Ma, J. He, Ultrafast and ultrasensitive phototransistors based on few-layered HfSe₂. *Appl. Phys. Lett.* **109**, 213105 (2016).
- M. Kang, S. Rathi, I. Lee, L. Li, M. A. Khan, D. Lim, Y. Lee, J. Park, S. J. Yun, D.-H. Youn, C. Jun, G.-H. Kim, Tunable electrical properties of multilayer HfSe₂ field effect transistors by oxygen plasma treatment. *Nanoscale* **9**, 1645–1652 (2017).
- D. L. Greenaway, R. Nitsche, Preparation and optical properties of group IV–V₂ chalcogenides having CdI₂ structure. *J. Phys. Chem. Solids* **26**, 1445–1458 (1965).
- M. L. Schultz, Silicon: Semiconductor properties. *Infrared Phys.* **4**, 93–112 (1964).
- P. Tsipas, D. Tsoutsou, J. Marquez-Velasco, K. E. Aretouli, E. Xenogiannopoulou, E. Vassalou, G. Kordas, A. Dimoulas, Epitaxial ZrSe₂/MoSe₂ semiconductor v.d. Waals heterostructures on wide band gap AlN substrates. *Microelectron. Eng.* **147**, 269–272 (2015).
- K. E. Aretouli, P. Tsipas, D. Tsoutsou, J. Marquez-Velasco, E. Xenogiannopoulou, S. A. Giamini, E. Vassalou, N. Kelaidis, A. Dimoulas, Two-dimensional semiconductor HfSe₂ and MoSe₂/HfSe₂ van der Waals heterostructures by molecular beam epitaxy. *Appl. Phys. Lett.* **106**, 143105 (2015).
- A. V. Krukav, A. V. Vydrov, A. F. Izmaylov, G. E. Scuseria, Influence of the exchange screening parameter on the performance of screened hybrid functionals. *J. Chem. Phys.* **125**, 224106 (2006).
- J. von Boehm, H. M. Isomaki, Relativistic p-d gaps of 1T TiSe₂, TiS₂, ZrSe₂ and ZrS₂. *J. Phys. C Solid State Phys.* **15**, L733–L737 (1982).
- A. W. Tsen, R. Hovden, D. Wang, Y. D. Kim, J. Okamoto, K. A. Spoth, Y. Liu, W. J. Lu, Y. P. Sun, J. C. Hone, L. F. Kourkoutis, P. Kim, A. N. Pasupathy, Structure and control of charge density waves in two-dimensional 1T-TaS₂. *Proc. Natl. Acad. Sci. U.S.A.* **112**, 15054–15059 (2015).
- M. J. Mleczko, R. L. Xu, K. Okabe, H.-H. Kuo, I. R. Fisher, H.-S. P. Wong, Y. Nishi, E. Pop, High current density and low thermal conductivity of atomically thin semimetallic WTe₂. *ACS Nano* **10**, 7507–7514 (2016).
- J.-Y. J. Lin, A. M. Roy, A. Nainani, Y. Sun, K. C. Saraswat, Increase in current density for metal contacts to n-germanium by inserting TiO₂ interfacial layer to reduce Schottky barrier height. *Appl. Phys. Lett.* **98**, 092113 (2011).
- W. Park, Y. Kim, S. K. Lee, U. Jung, J. H. Yang, C. Cho, Y. J. Kim, S. K. Lim, I. S. Hwang, H.-B.-R. Lee, B. H. Lee, Contact resistance reduction using Fermi level de-pinning layer for MoS₂ FETs, in *IEEE International Electron Devices Meeting (IEDM)* (IEEE, 2014), pp. 5.1.1–5.1.4.
- S. Lee, A. Tang, S. Aloni, H.-S. P. Wong, Statistical study on the Schottky barrier reduction of tunneling contacts to CVD synthesized MoS₂. *Nano Lett.* **16**, 276–281 (2016).
- Y. J. Kim, Y. G. Lee, U. Jung, S. Lee, S. K. Lee, B. H. Lee, A facile process to achieve hysteresis-free and fully stabilized graphene field-effect transistors. *Nanoscale* **7**, 4013–4019 (2015).
- S. Das, H.-Y. Chen, A. V. Penumatcha, J. Appenzeller, High performance multilayer MoS₂ transistors with scandium contacts. *Nano Lett.* **13**, 100–105 (2013).
- S. Mañas-Valero, V. García-López, A. Cantarero, M. Galbiati, Raman spectra of ZrS₂ and ZrSe₂ from bulk to atomically thin layers. *Appl. Sci.* **6**, 264 (2016).
- S. Arulkumaran, Z. H. Liu, G. I. Ng, W. C. Cheong, R. Zeng, J. Bu, H. Wang, K. Radhakrishnan, C. L. Tan, Temperature dependent microwave performance of AlGaIn/GaN high-electron-mobility transistors on high-resistivity silicon substrate. *Thin Solid Films* **515**, 4517–4521 (2007).

45. P. Kordoš, D. Donoval, M. Florovič, J. Kováč, D. Gregušová, Investigation of trap effects in AlGaIn/GaN field-effect transistors by temperature dependent threshold voltage analysis. *Appl. Phys. Lett.* **92**, 152113 (2008).
46. M. Ľapajna, K. Čičo, J. Kuzmík, D. Pogany, G. Pozzovivo, G. Strasser, J. F. Carlin, N. Grandjean, K. Fröhlich, Thermally induced voltage shift in capacitance-voltage characteristics and its relation to oxide/semiconductor interface states in Ni/Al₂O₃/InAlN/GaN heterostructures. *Semicond. Sci. Technol.* **24**, 035008 (2009).
47. G. Lucovsky, R. M. White, J. A. Benda, J. F. Revelli, Infrared-reflectance spectra of layered group-IV and group-VI transition-metal dichalcogenides. *Phys. Rev. B* **7**, 3859–3870 (1973).
48. S. Das, J. Appenzeller, Where does the current flow in two-dimensional layered systems? *Nano Lett.* **13**, 3396–3402 (2013).
49. H. Liu, P. D. Ye, MoS₂ dual-gate MOSFET with atomic-layer-deposited Al₂O₃ as top-gate dielectric. *IEEE Electron Dev. Lett.* **33**, 546–548 (2012).
50. K. Choi, S. R. A. Raza, H. S. Lee, P. J. Jeon, A. Pezeshki, S.-W. Min, J. S. Kim, W. Yoon, S.-Y. Ju, K. Leec, S. Im, Trap density probing on top-gate MoS₂ nanosheet field-effect transistors by photo-excited charge collection spectroscopy. *Nanoscale* **7**, 5617–5623 (2015).
51. X. Cui, G.-H. Lee, Y. D. Kim, G. Arefe, P. Y. Huang, C.-H. Lee, D. A. Chenet, X. Zhang, L. Wang, F. Ye, F. Pizzocchero, B. S. Jessen, K. Watanabe, T. Taniguchi, D. A. Muller, T. Low, P. Kim, J. Hone, Multi-terminal transport measurements of MoS₂ using a van der Waals heterostructure device platform. *Nat. Nanotechnol.* **10**, 534–540 (2015).
52. S. Xu, Z. Wu, H. Lu, Y. Han, G. Long, X. Chen, T. Han, W. Ye, Y. Wu, J. Lin, J. Shen, Y. Cai, Y. He, F. Zhang, R. Lortz, C. Cheng, N. Wang, Universal low-temperature Ohmic contacts for quantum transport in transition metal dichalcogenides. *2D Mater.* **3**, 021007 (2016).
53. C. Gong, H. J. Zhang, W. H. Wang, L. Colombo, R. M. Wallace, K. J. Cho, Band alignment of two-dimensional transition metal dichalcogenides: Application in tunnel field effect transistors. *Appl. Phys. Lett.* **103**, 053513 (2013).
54. W. X. Zhang, Z. S. Huang, W. L. Zhang, Y. R. Li, Two-dimensional semiconductors with possible high room temperature mobility. *Nano Res.* **7**, 1731–1737 (2014).
55. J. P. Perdew, K. Burke, M. Ernzerhof, Generalized gradient approximation made simple. *Phys. Rev. Lett.* **77**, 3865–3868 (1996).
56. G. Mirabelli, C. McGeough, M. Schmidt, E. K. McCarthy, S. Monaghan, I. M. Povey, M. McCarthy, F. Gity, R. Nagle, G. Hughes, A. Cafolla, P. K. Hurley, R. Duffy, Air sensitivity of MoS₂, MoSe₂, MoTe₂, HfS₂, and HfSe₂. *J. Appl. Phys.* **120**, 125102 (2016).
57. H. Li, G. Lu, Y. L. Wang, Z. Y. Yin, C. X. Cong, Q. Y. He, L. Wang, F. Ding, T. Yu, H. Zhang, Mechanical exfoliation and characterization of single- and few-layer nanosheets of WSe₂, TaS₂, and TaSe₂. *Small* **9**, 1974–1981 (2013).
58. P. Barberis, T. Merle-Mejean, P. Quintard, On Raman spectroscopy of zirconium oxide films. *J. Nucl. Mater.* **246**, 232–243 (1997).

Acknowledgments: Experimental work was performed at the Stanford Nanofabrication Facility and Stanford Nano Shared Facilities. ARPES studies were conducted at the Advanced Light Source of Lawrence Berkeley National Laboratory; cross-sectional TEM of device samples was performed by Evans Analytical Group. We acknowledge fruitful discussions with J. Provine, M. Rincon, and J. Conway, and technical assistance from J. McVittie (evaporator vacuum transfer chamber), C. English (pulsed measurements and TLM analysis), and K. Smithe (ALD oxide characterization). **Funding:** This work was supported, in part, by the Air Force Office of Scientific Research grant FA9550-14-1-0251, the NSF EFRI 2-DARE grant 1542883, the Stanford Initiative for Novel Materials and Processes (INMP), and the Department of Energy (DOE), Office of Basic Energy Sciences, Division of Material Sciences. Crystal growth (I.R.F. and H.-H.K.) was supported by the DOE, Office of Basic Energy Sciences under contract DE-AC02-76SF00515. B.M.-K. acknowledges the computational awards received on the XSEDE (Extreme Science and Engineering Discovery Environment) project supported by NSF and on the Carbon cluster of Center for Nanoscale Materials supported by the DOE, Office of Basic Energy Sciences under contract no. DE-AC02-06CH11357. M.J.M. would like to acknowledge a Natural Sciences and Engineering Research Council (NSERC) Postgraduate Scholarships–Doctoral fellowship. **Author contributions:** M.J.M., Y.N., and E.P. designed the experiments. H.-H.K. and M.J.M. grew bulk crystals under the supervision of I.R.F. M.J.M. fabricated, measured, and assessed devices, preparing cross-sectional TEM samples with H.R.L. B.M.-K. performed DFT calculations. C.Z., R.G.M., and Z.-X.S. conducted ARPES studies of the grown crystals. M.J.M. and E.P. wrote the manuscript with contributions from B.M.-K. and C.Z. All authors reviewed and commented on the final draft. **Competing interests:** The authors declare that they have no competing interests. **Data and materials availability:** All data needed to evaluate the conclusions of this study are present in the paper and/or the Supplementary Materials. Additional data related to this paper may be requested from the authors.

Submitted 14 February 2017

Accepted 12 July 2017

Published 11 August 2017

10.1126/sciadv.1700481

Citation: M. J. Mleczko, C. Zhang, H. R. Lee, H.-H. Kuo, B. Magyari-Köpe, R. G. Moore, Z.-X. Shen, I. R. Fisher, Y. Nishi, E. Pop, HfSe₂ and ZrSe₂: Two-dimensional semiconductors with native high-κ oxides. *Sci. Adv.* **3**, e1700481 (2017).